Molecular-dynamics simulations of epitaxial crystal growth from the melt. I. Si(100)

Uzi Landman, W. D. Luedtke, M. W. Ribarsky, R. N. Barnett, and C. L. Cleveland
School of Physics, Georgia Institute of Technology, Atlanta, Georgia 30332
(Received 27 July 1987)

Liquid-phase epitaxial growth onto a Si(100) substrate is studied using molecular-dynamics simulations. The material is described using two- and three-body interaction potentials which provide a realistic description of crystalline silicon and of the crystal-melt interface. After preparation at solid-melt coexistence, the system is driven out of equilibrium by allowing the conduction of heat to the underlying substrate. Under these conditions the system initially undercools, and subsequently crystallization and growth occur at an overall rate of 18 m/sec, resulting in a perfect crystal. The faceted morphology of the solid-melt interface, characterized by a predominance of (111) microfacets, is maintained throughout the fast-crystallization stage. The dynamics of the crystal-growth process is investigated with refined spatial and temporal resolution via monitoring of real-space particle trajectories and of the evolution of system characteristics such as temperature, potential-energy, and density profiles.

I. INTRODUCTION

Understanding the mechanisms, kinetics, and dynamics of crystal-growth processes and identification of the microscopic material properties and of the macroscopic control parameters related to the method of growth, which govern the growth processes and quality of the grown crystals, are of fundamental importance from both basic and applied perspectives. These issues, therefore, provide the motivation for extensive experimental and theoretical research of these phenomena.[1-10] Indeed, advances in experimental techniques and improved theoretical methods have led to marked enhancement of our knowledge of crystal-growth processes, with a focus on refinements of the temporal and spatial resolution with which these phenomena can be studied. Among the various crystal-growth techniques, one of the oldest is growth from the melt, or liquid-phase epitaxy (LPE).[11] The advent of fast, pulsed-laser annealing techniques[3-10] opened a new era in crystal-growth technology, as well as in the theoretical understanding of the microscopics of melting and solidification processes. Though numerous kinetic models of solidification have been proposed and investigated, the complexity of the problem renders it extremely difficult to formulate and implement detailed, accurate, analytical models. On the other hand, these systems are suited for computer modeling, particularly computer simulations, which afford systematic probing of the microscopic structure and dynamics of equilibrium and nonequilibrium liquid-solid interfaces[12-21] and thus of crystal-growth processes. Timely advances in experimental studies of fast solidification processes and in computational capabilities, along with improvements in our understanding of the energetics and nature of interactions and bonding of materials and in our ability to model them, provide the motivation for intensive investigations, using computer simulations, of the principles of crystal growth of materials of technological relevance, semiconductors in particular. Having studied in the past[17] the nature of the *equilibrium* liquid-solid interface of silicon, using interaction potentials[22] which provide a rather faithful description of this material, we explore in this paper[23] the dynamics of LPE of silicon, i.e., the structure and dynamics of the *nonequilibrium* interface. Since in LPE two condensed phases (solid and liquid) interact with one another (with the interaction driving a phase transformation of the liquid) it is important that the dynamical nature of the two phases be incorporated in the theoretical model of the growth process. Molecular-dynamics simulations are ideally suited for this situation since the dynamics of all particles of the system is followed throughout the calculation, thus allowing for cooperative dynamical effects originating from the condensed-phase nature of the system.

As in the case of the equilibrium interface where we discovered[17] (theoretically and experimentally) structural anisotropies [i.e., a faceted (001) interface, as opposed to a flat (111) interface] depending on the orientation of the interface, we find that the rate of crystal growth as well as the quality of the grown crystal and the type of defects which develop depend on the crystallographic orientation and on the rate of heat transfer to the substrate. From an equilibrated system at solid-melt coexistence, growth is initiated by driving the system out of the equilibrium state via allowing heat conduction to the substrate at a chosen rate. Crystallization does not start until the temperature at the interface drops from the initial melting-point temperature by about 150 K. Once the interface region supercools to this degree, ordering and crystallization processes start to occur. The liquid-phase epitaxial growth occurs most rapidly on the (001) surface, yielding a perfect single crystal at a growth velocity of ~ 18 m/sec, while growth on the (111) surface (discussed in the following paper) driven by the same rate of heat removal as for the (001) system yields an imperfect crystal containing an assortment of defects (stacking faults, single defects, and disordered regions), at a growth velocity of ~ 14 m/sec. [As shown in the following paper, the per-

fection of the grown crystal on the (111) surface is markedly improved when the growth rate is slowed down to ~9 m/sec.] Additionally, we observe that the morphology of the crystal-melt interface maintains a microfaceted structure similar to that found in the equilibrium state. Furthermore, we find that growth from the melt involves cooperative processes, related to the structure and dynamics of the melt in the vicinity of the growth front, and self-annealing processes, which are responsible for the difference in the crystalline perfection in the (111) system for the two growth rates.

In Sec. II of the paper we describe the model interaction potentials which we employ in our calculations and the method of simulation. Our results for LPE on the (001) surface are described in Sec. III, and are discussed in the light of recent observations in Sec. IV.

II. INTERACTION POTENTIAL AND SIMULATION METHOD

The potential energy of a system of interacting particles can be written, in general, as a sum of contributions of varying order in the number of particles (one-body, two-body, and higher-order terms). Because of the directional, covalent bonding characteristic of tetrahedral semiconductors, a model of the potential for these materials must go beyond the often-used pair interactions. This is achieved via the inclusion of nonadditive, angle-dependent contributions which describe three-body and higher-order interactions.[22]

In our simulations we have employed optimized two- and three-body potentials, V_2 and V_3, respectively:

$$v_2(r_{ij}) = A\,(Br_{ij}^{-P} - 1)g_\beta(r_{ij}) \equiv v_{ij} \ , \tag{1a}$$

$$v_3(\mathbf{r}_i,\mathbf{r}_j,\mathbf{r}_k) = v_{jik} + v_{ijk} + v_{ikj} \ , \tag{1b}$$

$$v_{jik} = \lambda g_\gamma(r_{ij}) g_\gamma(r_{ik})(\cos\theta_{jik} + \tfrac{1}{3})^2 \ , \tag{1c}$$

where r_{ij} is the distance between atoms i and j, and $g_\gamma(r) = \exp[\gamma/(r-a)]$ for $r < a$ and vanishes for $r \geq a$. In Eqs. (1), r is expressed in units of $\sigma = 0.209\,51$ nm, the unit of energy is $\varepsilon = 50$ kcal/mol, and that of temperature is $T = \varepsilon/k_B$ (to convert to T in K multiply the reduced temperature by 2.517×10^4); $A = 7.049\,556\,277$, $B = 0.602\,224\,558\,4$, $P = 4$, $a = 1.8$, $\lambda = 21$, $\beta = 1$, and $\gamma = 1.2$. The time unit, t.u., is $\sigma(m/\varepsilon)^{1/2} = 7.6634 \times 10^{-14}$ sec. As seen from Eq. (1c), the three-body contribution to the potential energy vanishes for the perfect tetrahedral angle. Therefore, the liquid is characterized by a higher magnitude of V_3 than the solid. These potentials have been shown[22,24] to describe adequately various properties of bulk solid and liquid Si and have been used by us[17] and others[18] previously in studies of the equilibrium interface between (100) and (111) crystalline Si and its melt.

Customarily, molecular-dynamics simulations employ a constant-volume computational cell which is then repeated in space using periodic boundary conditions. However, in order to allow for situations which involve changes in material density and structure in a dynamical manner, it is necessary to regard the vectors defining the calculational cell as dynamical variables, i.e., formulate a nonconstant-volume molecular-dynamics method.[25] In our simulations we have adopted the ansatz Lagrangian formulation,[25] which we extended to include three-body interactions.

In the constant-external-pressure molecular-dynamics (MD) formulation the position vectors of the particles inside the calculational cell, $\mathbf{r}_i$ ($i = 1, \ldots, N$), are rewritten in terms of scaled coordinates,

$$\mathbf{s}_i = (\xi,\eta,\zeta) \quad \text{with } 0 \leq \xi < 1,\ 0 \leq \eta < 1,\ 0 \leq \zeta < 1 \ ,$$

$$\mathbf{r}_i = \mathbf{a}\xi + \mathbf{b}\eta + \mathbf{c}\zeta \ , \tag{2}$$

where **a**, **b**, and **c** are three *time-dependent* vectors which span the calculational cell (an arbitrary parallelepiped). Defining the matrix $\underline{H} \equiv (\mathbf{a},\mathbf{b},\mathbf{c})$, whose columns are given by the components of the vectors **a**, **b**, and **c**, Eq. (2) is written as

$$\mathbf{r}_i = \underline{H}\mathbf{s}_i \ . \tag{3}$$

The volume of the calculational cell, Ω, is given by $\det\underline{H}$ and the distance between particles i and j is given in terms of the metric tensor $\overleftrightarrow{G} = \underline{H}^T\underline{H}$, where $\underline{H}^T$ denotes the transpose of $\underline{H}$, by

$$(\mathbf{r}_i - \mathbf{r}_j)^2 = (\mathbf{s}_i - \mathbf{s}_j)^T \cdot \overleftrightarrow{G} \cdot (\mathbf{s}_i - \mathbf{s}_j) \ . \tag{4}$$

Following Parrinello and Rahman,[25] we write the ansatz Lagrangian

$$L = \tfrac{1}{2}\sum_i m_i \dot{\mathbf{s}}_i^T \cdot \overleftrightarrow{G} \cdot \dot{\mathbf{s}}_i - V - P_{\text{ext}}\Omega + \tfrac{1}{2}W\,\mathrm{Tr}\dot{\underline{H}}^T\dot{\underline{H}} \ , \tag{5}$$

where m_i is the mass of particle i, W is a constant having the dimension of mass, and V is the total interparticle potential [see Eqs. (1)],

$$V = \sum_{\substack{i\\(i<j)}}\sum_j v_2(r_{ij}) + \sum_{\substack{i\\(i<j<k)}}\sum_j\sum_k v_3(\mathbf{r}_i,\mathbf{r}_j,\mathbf{r}_k) \equiv V_2 + V_3 \ . \tag{6}$$

The equations of motion derived from the above Lagrangian are given by

$$m_i\underline{H}\ddot{\mathbf{s}}_i = -\sum_j \frac{\partial v_{ij}}{\partial \mathbf{r}_i} + \sum_j{}' \sum_k{}' \left[\frac{\partial v_{jik}}{\partial \mathbf{r}_j} - \frac{\partial v_{ijk}}{\partial \mathbf{r}_i}\right] - m_i(\underline{H}^T)^{-1}\dot{\overleftrightarrow{G}}\cdot\dot{\mathbf{s}}_i \ , \tag{7a}$$

and

$$W\ddot{\underline{H}} = (\overleftrightarrow{\Pi} - P_{\text{ext}}\overleftrightarrow{1})\Omega\cdot(\underline{H}^T)^{-1} \ , \tag{7b}$$

where the stress tensor $\overleftrightarrow{\Pi}$ is given by

$$\Omega\overleftrightarrow{\Pi} = \sum_i \left[m_i\mathbf{v}_i\mathbf{v}_i - \tfrac{1}{2}\sum_j{}' \frac{\partial v_{ij}}{\partial \mathbf{r}_i}\mathbf{r}_{ij} + \tfrac{1}{2}\sum_j{}'\sum_k{}' \left[\frac{\partial v_{jik}}{\partial \mathbf{r}_j} - \frac{\partial v_{ijk}}{\partial \mathbf{r}_i}\right]\mathbf{r}_{ij}\right] \ , \tag{7c}$$

where

$$\mathbf{v}_i = \underline{H}\dot{\mathbf{s}}_i \ . \tag{7d}$$

In the above equations the primed summations indicate

that terms where i, j, or k are equal are excluded. Interpreting $\tilde{\Pi}$ as the internal stress tensor, it is seen from Eq. (7b) that the time variation of $\underline{H}$, describing the dynamical MD calculational cell, is determined by the imbalance between the externally applied pressure P_{ext} and the instantaneous value of the internal stress in the system. The time scale of these variations is determined by the mass parameter W.

Since we are interested in an interface system possessing a free surface, our simulation system is constructed as a thick slab which is periodically repeated in two directions and is free (i.e., no periodic boundary conditions are imposed) in the third direction. Additionally, the slab is positioned on top of a static crystalline silicon substrate which is set up in the desired crystallographic orientation. The dimensions (and shape) of the two-dimensional (2D) calculational unit cell (including the static substrate) vary dynamically as described above, with $P_{\text{ext}}=0$ (for the box mass parameter we used $W=20$). As a consequence of the dynamical freedom of the density in our simulations, the internal pressure of the system fluctuates about zero. Ideally, one would like to construct a system where the solidification interface region and adjacent substrate which responds dynamically to the stresses which develop at the interface are coupled to a bulk subsystem (further spatially distant from the solidification region) whose characteristic response to the interfacial stresses is retarded and damped. However, the periodic-boundary conditions employed in molecular-dynamics simulations prevent such a construction. Furthermore, we expect that the influence of the above considerations on the energetics and structure and dynamical evolution of the system (particularly in the interfacial region) would be of reduced consequence due to the extent and small magnitude of the interfacial stress relative to that of the intermolecular interactions which underly the particle dynamics in the system.

In all our simulations we begin with a silicon crystal consisting of N_L dynamic layers with N_P particles per layer exposing either the (001) or the (111) faces (see the following paper). In simulations for the (001) system the Z axis was taken to be parallel to the [001] direction and the 2D cell is defined by the [110] and [$\bar{1}$10] directions. For this system $N_L=28$ and $N_P=36$ with four static substrate layers (i.e., the total number of dynamic particles was 1008). In the numerical integration of the equations of motion, using a fifth-order predictor-corrector algorithm, we employed an integration time step $\Delta t=0.015$ t.u. $=1.15\times10^{-3}$ psec; with this choice and a frequent updating of the interaction lists (every $8\Delta t$), the total energy of the system is conserved to at least six significant figures (for a few thousand time steps).

In each of the cases which we studied, the preparation procedure of the system was as follows: (i) The system was set up as a Si crystal in the desired configuration and was equilibrated at a reduced temperature of 0.064 (1593 K). (ii) A heat pulse was applied to the top $\frac{1}{3}$ of the system (from the vacuum side) via scaling of the particle velocities in that region to 0.19 (4782 K), and the system was allowed to evolve for 1.5×10^5 time steps ($\sim$175 psec). During this time the heat deposited via the heat pulse spreads over the whole system, raising its temperature to the melting point [$T_m=0.0662\pm0.0016$ (1665 K) compared to the experimental melting temperature of silicon, $T_m=0.0669\equiv1683$ K], and melting part of it (see Fig. 1 for evolution of the temperature and the three-body potential energy versus time during this stage). Thus, during this stage a system at equilibrium solid-melt coexistence is obtained. The system in this state is the starting point for the growth studies. (iii) The growth studies are performed by cooling at a desired rate (via scaling of velocities) the bottom two layers of the dynamic part of the system (i.e., those nearest the static substrate). That region is sufficiently far from the solid-melt interface to assure that the perturbation to the dynamics caused by the scaling of velocities does not influence the dynamics at the vicinity of the growth front. From our studies of the equilibrium solid-melt coexistence state, we determined [see Fig. 2(b) in Ref. 17 and Fig. 5 of this paper] that the average per particle potential energies in the liquid and solid regions are -1.78ε and -1.93ε ($\varepsilon=50$ kcal/mol) and thus our estimate of the per particle latent heat[26] is 0.15ε (31.4 kJ/mol). We have chosen a cooling rate (by scaling the velocities of particles in the bottom two layers every five time steps) such as to remove at a constant rate an amount of energy which is equal to the

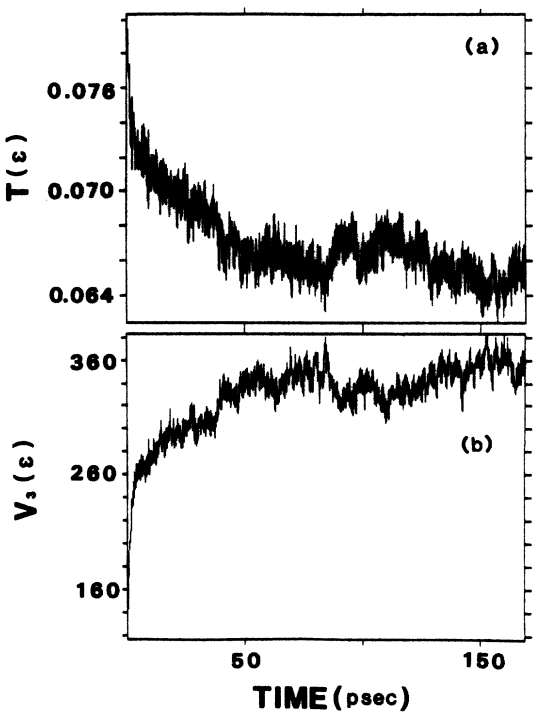

FIG. 1. Time development of the temperature, T, in units of ε, and total three-body potential energy for the system during the sample-preparation stage starting from the application of the heat pulse to the upper third of the system at $t=0$. Time is given in psec. Note the long times required to achieve equilibration. During this stage part of the system melts and an equilibrium solid-melt coexistence is achieved at the melting point $T_m=0.0662\pm0.0016$ (1665 K).

latent heat per layer ($N_P \times 0.15\varepsilon$) every 6 psec. Clearly this rate can be varied, as we have done in our studies of LPE on the (111) surface (see following paper).

In the following section we present our results for Si(100). Our results for growth on Si(111) are described in the following paper.

III. LIQUID-PHASE EPITAXY ON Si(001)

As we discussed previously,[17] the equilibrium crystal-melt interface in the (001) orientation exhibits a pronounced structure, with a tendency for the formation of microfacets established on (111) crystal planes, as demonstrated by the sample of particle trajectories, taken from our previous equilibrium studies,[17] shown in Fig. 2. These trajectories were recorded for $2000\Delta t$ and viewed along the $[\bar{1}10]$ direction (normal to the plane of the figure). The breakup of the interface into alternating (111) and $(\bar{1}\,\bar{1}\,1)$ crystalline planes is evident. Additionally, the melt region in the vicinity of the interface exhibits a degree of ordering due to the crystalline potential, resulting in a diffuseness of the interface in that region. In extended runs we observed that the morphology of the interface fluctuates [on a time scale of $\sim(4-5)\times 10^3\Delta t$] between equivalent facet configurations.

Starting from the equilibrated system at solid-melt coexistence (i.e., at T_m), the system is driven out of equilibrium by allowing heat conduction to the substrate as described in the preceding section. The time evolutions of the temperature, and of the three- and two-body contributions to the potential energy of the system during the growth stage, are shown in Fig. 3. As seen from this figure, in the first stage (up to ~ 25 psec) the system supercools [i.e., the temperature drops below the initial ($t=0$) melting point temperature]. At this initial stage no crystallization occurs, as is evident from the absence of trends in V_3 and V_2 and monitoring of the structure in the vicinity of the interface. The absence of noticeable crystallization during the initial cooling stage is demonstrated by the time development of V_2 and V_3 shown in Fig. 3 and the system profiles shown in Fig. 5. The sample particle trajectories recorded (over a time span of $3000\Delta t$) during the beginning of the cooling stage (~ 10 psec), shown in Fig. 4, exhibit the structured nature of the interface (in this figure the bottom layer is the fifth crystalline layer).

Detailed probing of the growth processes is provided via inspection of profiles of the particle densities, $\Delta n/\Delta Z^*$ versus Z^* along the [001] direction ($Z^*=1=18.14\sigma$), and via profiles of the per-particle potential energy, V_2+V_3, as well as those for the individual two-

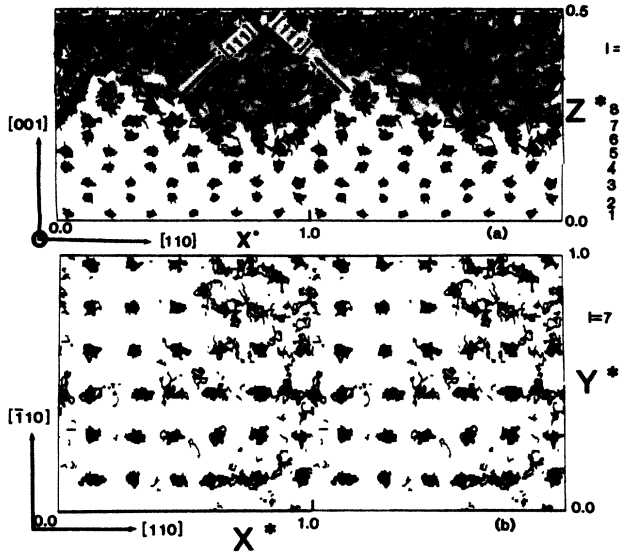

FIG. 2. Real-space particle trajectories, recorded over $2000\Delta t$, at the interface region, taken from our equilibrium studies (Ref. 17). The system is viewed along the $[\bar{1}10]$ direction. Distance is measured in units of $X^*=Y^*\equiv 10.9\sigma$ and $Z^*=1\equiv 18.14\sigma$. For the system used in that study the interface starts at about layer 6, as noted in the figure. Note the breakup of the interface into alternating (111) and $(\bar{1}\,\bar{1}\,1)$ crystalline planes forming microfacets. The 2D computational cell ($0\le X^*, Y^*\le 1$) is replicated along the X^*[110] direction to aid in visualization.

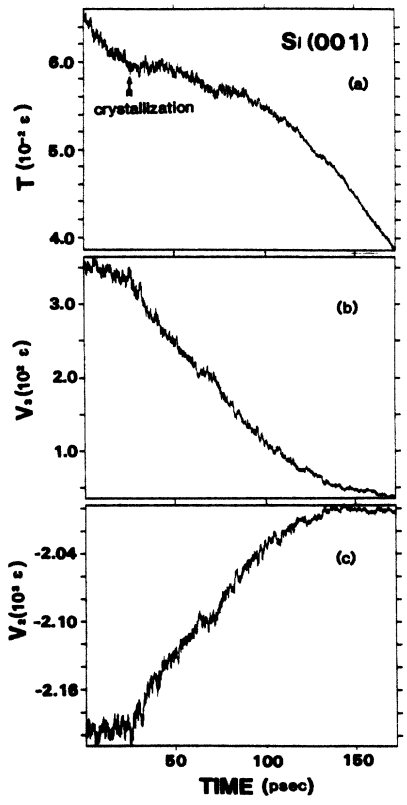

FIG. 3. Time development of the system temperature, T, in units of ε and of the per particle three- and two-body contributions to the potential energy throughout the growth simulation, beginning from the start of the heat extraction at $t=0$. The start of the crystallization stage is noted (~ 25 psec). Prior to this time the system cools down to below the initial-melting-point temperature.

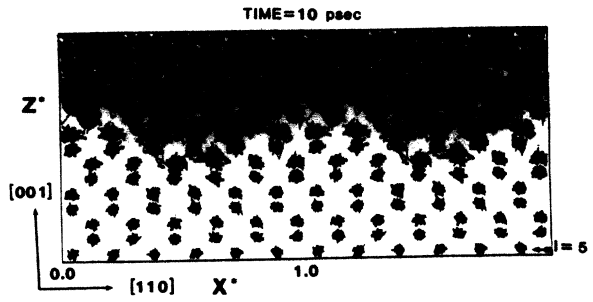

FIG. 4. Real-space particle trajectories at the interface region (starting in crystalline layer 5) recorded for $3000\Delta t$, at $t=10$ psec after the beginning of the growth simulation [i.e., during the cooling stage (see Fig. 3)]. The system is viewed along the $[\bar{1}10]$ direction. Distances are measured in units of $X^*=Y^*=11\sigma$ and $Z^*=18.14\sigma$. Note that the structured, microfaceted character of the interface maintains during the cooling stage. The 2D computational cell $(0\leq X^*, Y^*\leq 1)$ is replicated along the $X^*[110]$ direction to aid visualization.

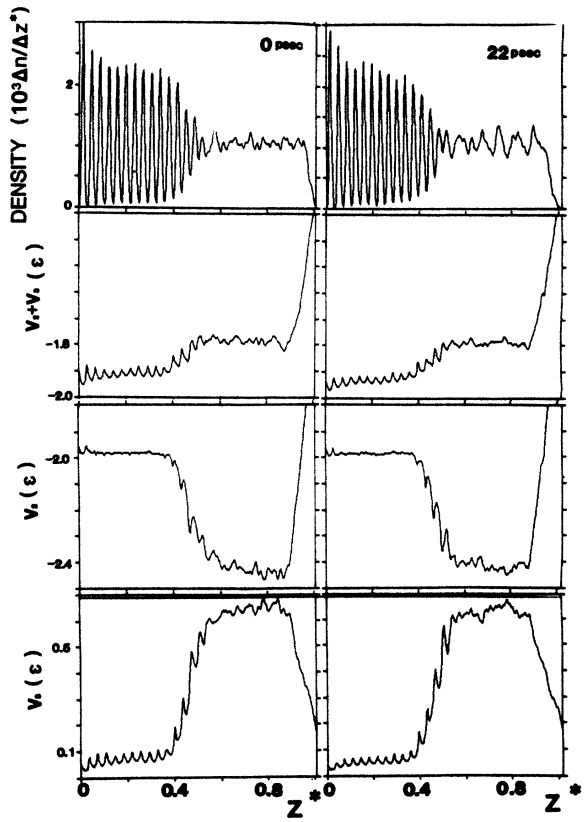

FIG. 5. Profiles of the particle density, $\Delta n/\Delta Z^*$, where Δn is the number of particles with Z^* coordinates between Z^* and $Z^*+\Delta Z^*$, and profiles of the per-particle total potential energy, V_2+V_3, and of the two- and three-body contributions vs Z^* $(Z^*=1\equiv 18.14\sigma)$, at $t=0$ and 22 psec. In the crystalline region, maxima in the density profiles and the corresponding minima in the potential-energy profiles occur at the crystalline layer positions. Note the diffuse character of the interface (see also Fig. 4). Comparison of the profiles for the two times demonstrates that no observable crystallization or ordering had occurred during the initial cooling stage.

and three-body contributions, taken at selected times during the simulation. The pronounced maxima in the density profiles and the corresponding minima in the potential-energy profiles correspond to the locations of crystalline, or partially crystalline, layers. Furthermore, we observe that the variation in the total potential energy, V_2+V_3, upon crossing from the solid to the melt regions is much smaller than the variation in the individual contributions, V_2 and V_3. We note that the positive contribution due to the three-body interaction is smaller in solid regions than in the liquid, as discussed before, while the contribution from the two-body potentials is less negative in the solid than in the liquid, which is consistent with the higher coordination number in the liquid. In addition, the absence during the simulations of particles in the vapor phase is consistent with the low experimental

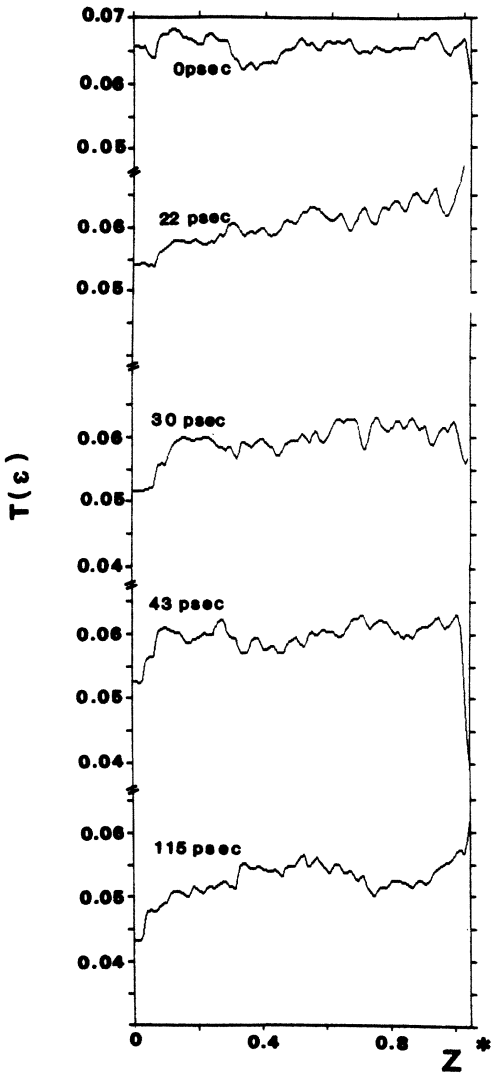

FIG. 6. Temperature, T, profiles of the system at selected times during the simulation. The $t=0$ profile was recorded for the equilibrium solid-melt coexistence system prior to the beginning of the growth simulation. All the profiles were obtained as short-time averages over $2\times 10^3\Delta t$.

triple-point pressure of $\sim 10^{-1}$ Pa.[26] Inspection of the sample profiles at $t=0$ and 22 psec, shown in Fig. 5, demonstrates that during this time period no noticeable structural development occurred. In particular, the solid-melt (diffuse) interface does not advance during the cooling stage, but continues to exhibit a diffuse, structured character.

Profiles of the system temperature (in units of ε) versus Z^* ($Z^*=1\equiv 18.14\sigma$) at selected times during the simulation are displayed in Fig. 6 [the temperature in a region of space containing N' particles is defined as $\frac{3}{2}N'k_BT=(1/2m)\sum_{i=1}^{N'}\mathbf{p}_i\cdot\mathbf{p}_i$]. These profiles were obtained as short-time averages ($2\times 10^3\Delta t$) and therefore they exhibit a certain degree of noise. Due to the dynamical evolution of the system, particularly the expulsion of latent heat which accompanies ordering and crystallization processes, we are forced to use such short averaging times. Comparison of the temperature profiles before the start of the heat conduction to the substrate ($t=0$) and toward the end of the initial cooling stage, $t=22$ psec, clearly illustrates the overall drop of the temperature throughout the system below the initial average temperature ($T_m=0.0662\pm 0.0016$, obtained by long-time averaging at the equilibrium state) and the development of a temperature gradient (see $t=22$ psec). It is seen that towards the end of the initial cooling stage ($t=22$ psec) the temperature of the interface region (see Figs. 3 and 5) drops to $\lesssim 0.06$, i.e., an undercooling of ~ 0.006 (or ~ 150 K). At about $t=25$ psec crystallization of the system starts at the solid-melt interaction (see Fig. 3).

In Figs. 7–9 we exhibit system profiles at selected times during the growth simulation. Comparison of the profiles shown in Fig. 7 for $t=0$ and 30 psec (compare also $t=22$ psec in Fig. 5) demonstrates the ordering processes which begin to take place at ~ 25 psec, signifying the start of the crystallization stage. The ordering at the interface region at $t=30$ psec is evidenced by a drop of V_3 for layers 14–16 and an enhancement in that region of the layered structure in the density profile. From the temperature profile shown in Fig. 6 we find that at that time the temperature at the interface region is below 0.06. Inspection of the evolution of the system during the subsequent 13 psec, shown in Fig. 8, demonstrates the "explosive" nature of the epitaxial crystallization process in this system, once it starts. We observe that the diffuse nature of the interface, characterized by the gradual transition in the potential-energy profiles between the crystalline and melt regions, maintains during the crystallization process. An added complication in attempting to locate

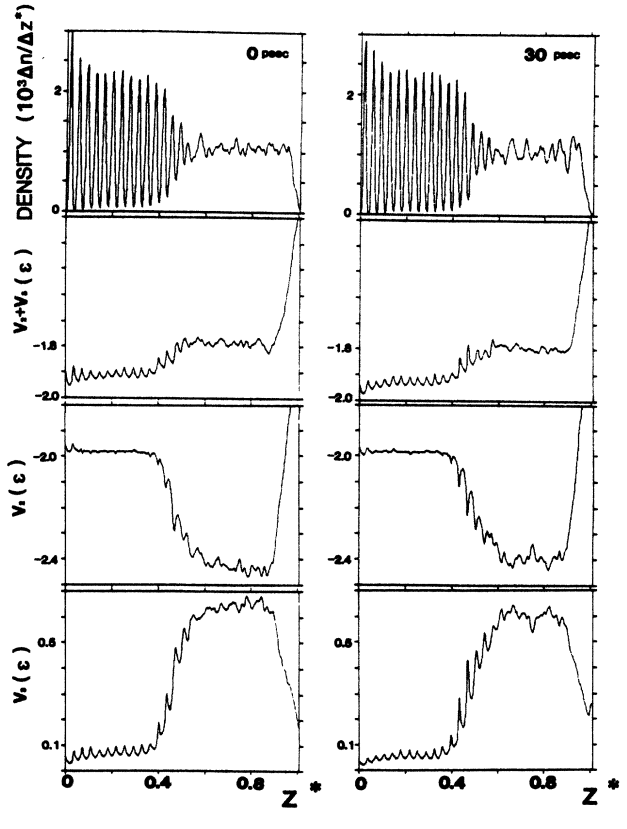

FIG. 7. Profiles of the system particle density, of the per-particle total potential energy V_2+V_3, and of the two-body, V_2, and three-body, V_3, contributions at the start of the growth simulation $t=0$, and shortly after the start of crystallization, $t=30$ psec (see Fig. 3). See caption to Fig. 5 for further detail.

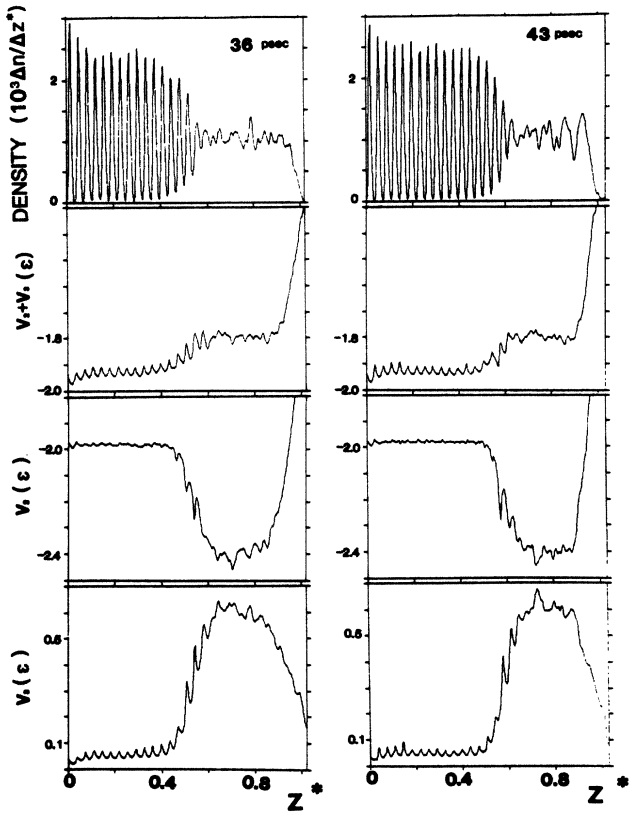

FIG. 8. Same as Fig. 7 for $t=36$ and 43 psec, illustrating the evolution of the system during growth.

the interface in the system under study is the structured (microfaceted or rough) nature of the interface. Nevertheless, an estimate of the rate of growth can be obtained by following the time development of minima in V_3 (or V_2) and features in the density profiles. Following the evolution of the system from $t=30$ to 43 psec, we estimate that the crystallization front advanced during this time span by about two crystalline layers. Since the layer spacing is about 1.3 Å, we obtain a crystallization rate of ~ 20 m/sec (when the overall growth process is used in these estimates, a rate of ~ 18 m/sec is obtained). Additionally, we remark that during the fast crystalline growth the temperature at the solidification front remains at or below 0.06.

Since the crystalline-melt interface at equilibrium (see Fig. 2) and during the initial cooling stage (see Fig. 4) exhibits a characteristic microfaceted morphology, it is of interest to inquire about the interface morphology, and the time scale of its variations, during growth. In Fig. 10(a) we show real-space particle trajectories in the interface region recorded during the fast-growth stage in the time period 51–58 psec (see Fig. 3), viewed from the $[\bar{1}10]$ direction. The rough nature of the crystalline-melt interface and the prevalence of (111) planes is evident from the figure. Furthermore, in Figs. 10(b) and 10(c) we show contour plots of the per-particle three-body potential energy, for particles with $V_3 \leq 0.45\varepsilon$. [We have found that such contour plots can be used in order to separate solid from liquidlike regions (the shape of the surface contours does not depend strongly on the cutoff value, in the vicinity of 0.45ε).] These contours were obtained as averages for the time intervals 50.5–51.5 psec [Fig. 10(b)] and 55.5–56.5 psec [Fig. 10(c)]. These potential contours complement and corroborate the picture of the interface morphology. In addition, since the time period separating the two contour plots in Figs. 10(b) and 10(c) corresponds roughly to the time that it takes for the crystalline phase to advance by one layer spacing, it gives an idea about the structural and temporal characteristics of the microscopic changes in the interface morphology during growth. To complete the characterization of the

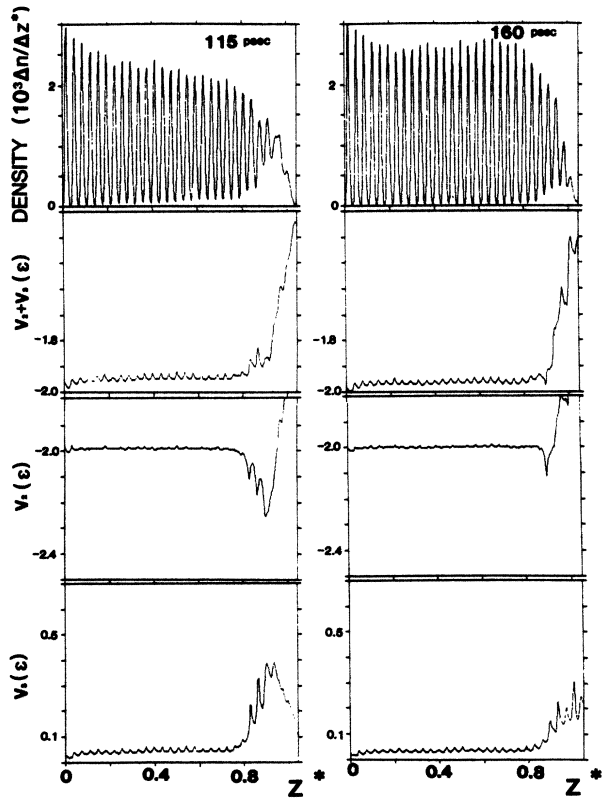

FIG. 9. Same as Fig. 7 for $t=115$ and 160 psec, at the end of the fast crystallization process and at the final stage of the simulation, respectively.

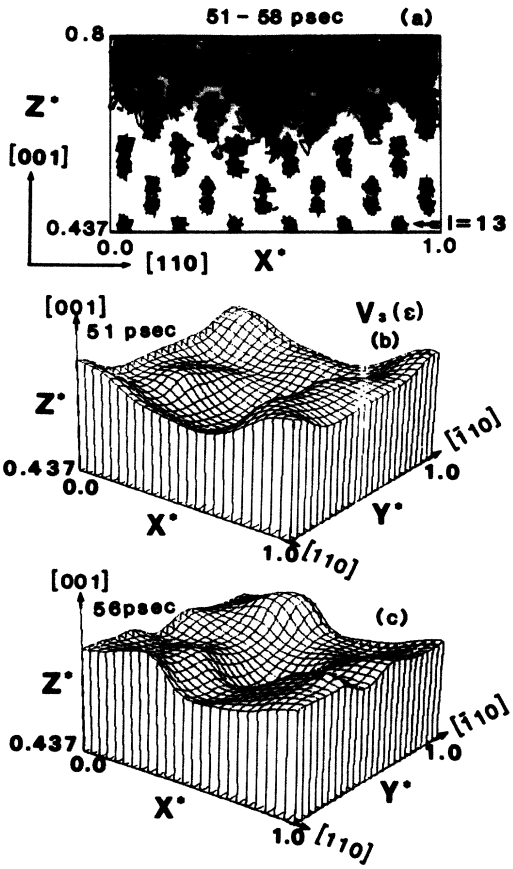

FIG. 10. (a) Real-space particle trajectories at the interface region, starting at crystalline layer number 13, recorded during the fast growth stage in the time span 51–58 psec (about the time period for growth of one crystalline layer). The system is viewed along the $[\bar{1}10]$ direction and length is in the units given in the caption to Fig. 4. The figure demonstrates that the structured character of the interface maintains during the fast crystallization process (compare Figs. 2 and 4). (b) Contour plot of V_3, recorded at 50.5–51.5 psec, for particles with per particle $V_3 \leq 0.45\varepsilon$, exhibiting the morphology of the interface between the solid region of the sample and the melt (which possess per-particle V_3 values greater than 0.45ε). (c) Same as (b), recorded towards the end of the time interval shown in (a), 55.5–56.5 psec. Comparison of (b) and (c) illustrates the manner in which the interface morphology varies during growth of a layer.

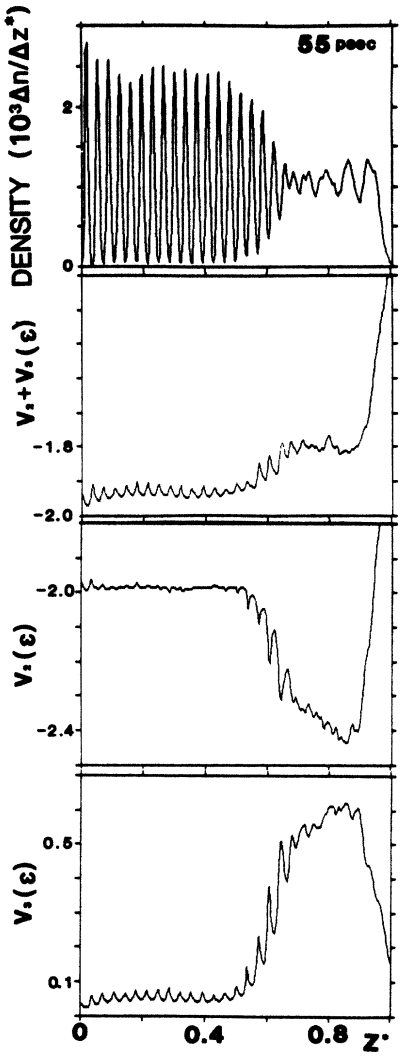

FIG. 11. Profiles of the system particle density, of the particle total potential energy, V_2+V_3, and of the two-body, V_2, and three-body, V_3, contributions during the fast growth process, at 55 psec.

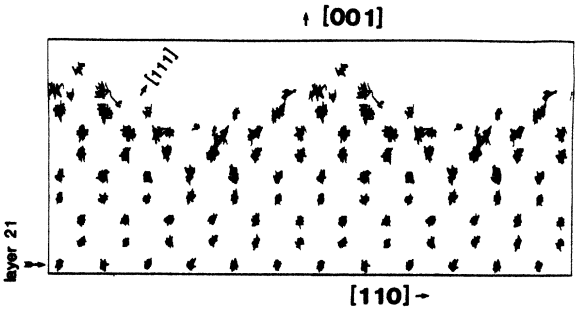

FIG. 12. Real-space particle trajectories of the system, starting at crystalline layer 21, at the end of the growth-simulation study $t=160$ psec, recorded for $3000\Delta t$, demonstrating a structured, microfaceted, crystalline-vacuum interface with a tendency to form (111) planes. The system is viewed from the [001] direction. The units of length as in Fig. 4. The 2D computational cell ($0\leq X^*, Y^*\leq 1$) was replicated along the X^* [110] direction to aid visualization.

system at this stage of growth, we display in Fig. 11 the system profiles at $t=55$ psec.

In Fig. 9 we show the system profiles at the final stages of the growth process (115 psec; see also Fig. 3) and close to the end of the simulation (160 psec). As seen from the figure, at $t=115$ psec most of the system has crystallized and the temperature dropped to below 0.055 (see Fig. 6). The final stages of the process involve structural refinement in the crystalline-vacuum interface region (see $t=160$ psec in Fig. 9). The final surface morphology of the grown crystal is shown in Fig. 12, exhibiting a faceted structure with a tendency to expose (111) and $(\bar{1}\,\bar{1}\,1)$ planes. The grown crystal possesses a high degree of structural perfection with no registry or intralayer defects.

IV. DISCUSSION

Laser-annealing techniques, i.e., the heating of a solid by high-power laser irradiation, offer novel methods for the preparation of materials and open new avenues in crystal-growth studies by allowing heating and cooling of the surface region of well-characterized materials with rates (and to temperatures) which are not attainable by other methods. It is now well accepted that the fast dissipation of the absorbed laser radiation by semiconductors (Si in particular) results in transient melting which leads to rapid solidification with solidification front velocities in the range of several meters per second. As such, the term laser annealing is tantamount to ultrafast liquid-phase epitaxy, since the mechanisms of solidification which occur subsequent to melting involve liquid and liquid-solid interface processes. Whereas in laser-annealing experiments the melt produced can be at a temperature which is above the melting temperature (depending on the laser-pulse duration and power), there is ample evidence that at the initial stages cooling to the melting point and below it (particularly in the vicinity of the solidification interface) must occur.[27] Therefore it is pertinent to discuss the results of our studies (where the starting point for the growth simulation is a system at solid-melt equilibrium, i.e., at the melting point) in light of the wealth of information obtained in laser-annealing investigations.[3–10]

Melting and solidification of single-component materials have been phenomenologically formulated using two models:[28] (i) the thermodynamic model[29,30] and (ii) the kinetic-rate-theory model.[31] Although both approaches are similar in many respects, the kinetic model can be better applied to nonequilibrium processes. According to this model an expression can be derived for the velocity of the melt-front propagation in terms of the rate, k_f, in which atoms leave the liquid and add to the solid, the latent heat of solidification L_c, the crystallization temperature T_c, the interface temperature T_i, and the degree of undercooling at the interface ΔT_i,

$$v=k_f\{1-\exp[-(L_c/k_BT_c)\Delta T_i/T_i]\}\ . \tag{8}$$

While for a slow, uniform, and small degree of undercooling (a situation for which the theory was originally constructed) T_i can be taken as the melting point, it is not

clear what value it should be assigned under the conditions applying to fast growth in the presence of large ΔT_i. Nevertheless, the above phenomenologically derived expression emphasizes the fundamental relationship between supercooling and the velocity of the phase transformation (solidification or melting). Considerations of the heat flow in a system undergoing a phase transformation emphasize, in addition, the dependence of the velocity of the interface on the heat gradient in the interface region.[28]

These theoretical models, which are based on a number of simplifying assumptions, motivated vast experimental efforts to measure and correlate growth velocities, undercooling, heat gradients, and thermodynamic properties of systems under laser-annealing growth conditions. These are immensely challenging experiments, and although a very large body of information has been accumulated, we cite only one experiment,[32] using transient conductance measurements, where the undercooling at an interface velocity of 6 m/sec has been deduced to be 90 K. From experiments[33–35] in which melting followed by solidification or amorphization occurs, it was concluded that at a velocity of 15 m/sec [above which growth on Si(001) yields an amorphous solid] the liquid must have a greater undercooling than 250 °C. Furthermore, in order to achieve such rapid growth it was estimated[34] that cooling rates in excess of 10^{11} °C/sec are achieved. In addition it was estimated[36] that the spatial gradients at the interface for melt-front velocities between 6 and 18 m/sec are in the range $(1.14-3.43)\times 10^7$ deg/cm. The values which we obtain from our simulations for the above characteristic growth parameters are the following: The cooling rate (see end of Sec. II) which we employed corresponds to $\sim 2\times 10^{12}$ K/sec, the temperature gradient at the start of the crystallization process (see temperature profile at $t=30$ psec in Fig. 6) is estimated as $(5-7)\times 10^8$ K/cm, and the average growth velocity, resulting in a perfect grown crystal, is 18 m/sec. These values, which are in general good agreement with those deduced from experimental data and analyses of phenomenological growth models, lend strong support as to the realistic merits of our simulations and the interaction potentials[22] which were employed.

The growth mode which we observed and analyzed emphasizes the dynamical nature of the two interacting phases (solid and melt), the kinetics of ordering processes in the melt in the vicinity of the moving interface,[13–15] and the interface morphology. Ample evidence exists, mainly through studies of silicon crystalline growth from the melt onto insulating substrates, and on Si(001) substrates, that the surface of crystalline silicon becomes faceted upon melting and that the solid-melt interface of a growing Si crystal establishes itself on the (111) crystal planes.[37] Furthermore, we have discussed previously[17] (see also Fig. 2) the faceted nature of the equilibrium, solid-melt coexistence Si(001) crystal-melt interface. In the present study we found that the microfaceted structure of the interface maintains even at a high-growth velocity.[38–40]

Finally, our observation that the crystal grown on the (001) silicon substrate at an average velocity of 18 m/sec is structurally perfect should be contrasted with the results which we obtained for LPE growth on Si(111), where the same rate of cooling resulted in a defective crystal grown at a velocity of 14 m/sec (see following paper). Indeed, the orientational dependence of high-speed silicon crystal growth from the melt has been observed experimentally,[41,42] demonstrating clearly that the maximum growth interface velocities for the formation of a defect-free crystal can be ordered in the orientation sequence $v(001)>v(011)>v(112)>v(111)$. We focus on these effects and offer further discussion in our following paper, where LPE on Si(111) is studied.

ACKNOWLEDGMENTS

This work was supported by the U.S. Department of Energy under Grant No. FG05-86ER45234 and in part by a grant from the North American Philips Corporation. The computations were performed on the Cray-XMP computer at the National Magnetic Fusion Energy Computer Center, Livermore, California.

[1] *Crystal Growth and Materials,* Vol. 2 of *Current Topics in Material Science,* edited by E. Kaldis and H. J. Scheel (North-Holland, Amsterdam, 1977).

[2] *Crystal Growth: A Tutorial Approach,* edited by W. Bardsley, D. T. J. Hurle, and J. B. Mullin (North-Holland, Amsterdam, 1979).

[3] *Laser-Solid Interactions and Laser Processing—1978 (Materials Research Society, Boston),* proceedings of the Symposium on Laser-Solid Interactions and Laser Processing, AIP Conf. Proc. No. 50, edited by S. D. Ferris, H. J. Leamy, and J. M. Poate (AIP, New York, 1979).

[4] *Laser and Electron-Beam Interactions with Solids,* edited by B. R. Appleton and G. K. Celler (North-Holland, Amsterdam, 1982).

[5] *Laser-Solid Interactions and Transient Thermal Processing of Materials,* edited by J. Narayan, W. L. Brown, and R. A. Lemons (North-Holland, Amsterdam, 1983).

[6] *Energy Pulse Modifications of Semiconductors and Related Materials,* edited by K. Hennig (Akademie der Wissenschaften der DDR, Rossendorf, 1984), Vols. 1 and 2.

[7] *Laser Annealing of Semiconductors,* edited by J. M. Poate and J. W. Mayer (Academic, New York, 1982).

[8] *Pulsed Laser Processing of Semiconductors,* Vol. 23 of *Semiconductors and Semimetals,* edited by R. F. Wood, C. W. White, and R. T. Young (Academic, Orlando, 1984).

[9] See review by K. A. Jackson, in *Surface Modification and Alloying,* edited by J. M. Poate, G. Foti, and D. C. Jacobsen (Plenum, New York, 1983), Chap. 3.

[10] See review by J. M. Poate, J. Cryst. Growth **79**, 549 (1986).

[11] See review by J. C. Brice, in *Crystal Growth and Materials,* Ref. 1, p. 571.

[12] See references in a review by F. F. Abraham, J. Vac. Sci.

Technol. B **2**, 534 (1984); see articles in *Fluid Interfacial Phenomena,* edited by C. A. Croxton (Wiley, Chichester, 1986); U. Landman, R. N. Barnett, C. L. Cleveland, W. D. Luedtke, M. W. Ribarsky, D. Scharf, and J. Jortner, Mater. Res. Soc. Symp. Proc. **63**, 273 (1985).

[13]U. Landman, C. L. Cleveland, and C. S. Brown, Phys. Rev. Lett. **45**, 2032 (1980); U. Landman, C. L. Cleveland, C. S. Brown, and R. N. Barnett, in *Nonlinear Phenomena of Phase Transitions and Instabilities,* edited by T. Riste (Plenum, New York, 1982), p. 379.

[14]C. L. Cleveland, U. Landman, and R. N. Barnett, Phys. Rev. Lett. **49**, 790 (1982).

[15]U. Landman, R. N. Barnett, C. L. Cleveland, R. H. Rast, J. Vac. Sci. Technol. A **3**, 1574 (1985).

[16]J. Q. Broughton, G. H. Gilmer, and K. A. Jackson, Phys. Rev. Lett. **49**, 1496 (1982).

[17]U. Landman, W. D. Luedtke, R. N. Barnett, C. L. Cleveland, M. W. Ribarsky, E. Arnold, S. Ramesh, H. Baumgart, A. Martinez, and B. Khan, Phys. Rev. Lett. **56**, 155 (1986).

[18]F. F. Abraham and J. Q. Broughton, Phys. Rev. Lett. **56**, 734 (1986).

[19]R. F. Wood and G. E. Giles, Phys. Rev. B **23**, 2923 (1981); R. F. Wood, J. R. Kirkpatrick, and G. E. Giles, *ibid.* **23**, 555 (1981); R. F. Wood and G. A. Geist, Phys. Rev. Lett. **57**, 873 (1986); see also, articles in *Pulsed Laser Processing of Semiconductors,* in Ref. 8.

[20]M. O. Thompson and G. J. Galvin, in *Laser-Solid Interactions and Transient Thermal Processing of Materials,* Ref. 5, p. 57.

[21]P. Baeri, S. U. Campisano, G. Foti, and E. Rimini, Appl. Phys. Lett. **33**, 137 (1978); **50**, 788 (1979); see also Chap. 4 of *Laser Annealing of Semiconductors,* Ref. 7.

[22]F. H. Stillinger and T. A. Weber, Phys. Rev. B **31**, 5262 (1985).

[23]A preliminary report of this work was given in Bull. Am. Phys. Soc. **31**, 319 (1986).

[24]J. Q. Broughton and X. P. Li, Phys. Rev. B **35**, 9120 (1987); W. D. Luedtke and U. Landman, *ibid.* **37**, 4656 (1988).

[25]M. Parinello and A. Rahman, Phys. Rev. Lett. **45**, 1196 (1980).

[26]The experimental value of the latent heat is 50.7 kJ/mol (compare also the value of 30.3 kJ/mol obtained in Ref. 18); F. Roseburg, *Handbook of Electron Tube and Vacuum Techniques* (Addison-Wesley, Reading, Mass., 1965).

[27]See reviews in Chaps. 4 and 5 of *Pulsed Laser Processing of Semiconductors,* Ref. 8; also Ref. 10; Chap. 2 in *Laser Annealing of Semiconductors,* Ref. 7, and references cited therein.

[28]See review in Chap. 5 of *Pulsed Laser Processing of Semiconductors,* Ref. 8.

[29]D. Turnbull, in *Solid State Physics,* edited by F. Seitz and D. Turnbull (Academic, New York, 1956), Vol. 3, p. 225.

[30]See F. Spapen and D. Turnbull, in *Laser Annealing of Semiconductors,* Ref. 7, p. 15.

[31]B. Charlmers, Trans. AIME **200**, 519 (1954); K. A. Jackson and B. Charlmers, Can. J. Phys. **34**, 473 (1956).

[32]P. S. Pearcy and M. O. Thompson, in *Energy Beam-Solid Interactions and Transient Thermal Processing,* Mater. Res. Soc. Proc. **35**, edited by D. K. Bigelsen, G. Rozgonyi, and C. Shank (Materials Research Society, Pittsburgh, 1985), p. 53.

[33]P. L. Liu, R. Yen, N. Bloembergen, and R. T. Hodgson, Appl. Phys. Lett. **34**, 864 (1979).

[34]R. Tsu, R. T. Hodgson, T. Y. Yan, and J. E. E. Baglin, Phys. Rev. Lett. **42**, 1358 (1979).

[35]M. O. Thompson, J. W. Mayer, A. G. Cullis, H. C. Webber, N. G. Chew, J. M. Poate, and D. C. Jacobson, Phys. Rev. Lett. **50**, 896 (1983).

[36]See Chap. 4 in *Pulsed Laser Processing of Semiconductors,* Ref. 8, Table III, p. 218.

[37]G. K. Celler, K. A. Jackson, L. E. Trimble, Mc. D. Robinson, and D. J. Lischner, in *Energy Beam-Solid Interactions and Transient Thermal Processing,* edited by J. C. C. Fan and N. M. Johnson (North-Holland, New York, 1984), p. 409.

[38]M. W. Geis, H. J. Smith, B.-Y. Tsaur, J. C. C. Fan, D. J. Silversmith, and R. Mountain, J. Electrochem. Soc. **129**, 2813 (1982).

[39]K. F. Lee, T. J. Stultz, and J. F. Gibbons, in *Semiconductors and Semimetals,* edited by R. K. Willardson and A. C. Beer (Academic, New York, 1984), Vol. 17, p. 227.

[40]L. Pfieffer, S. Paine, G. H. Gilmer, W. van Saarloos, and K. W. West, Phys. Rev. Lett. **54**, 1944 (1985).

[41]J. M. Poate, Mater. Res. Soc. Symp. Proc. **4**, 121 (1982).

[42]A. G. Cullis, N. G. Chew, H. C. Weber, and D. J. Smith, J. Cryst. Growth **68**, 624 (1984).